Research Article

Showkat Ahmad Lone, Zehba Raizah, Anwar Saeed, and Gabriella Bognár*

Magnetized water-based hybrid nanofluid flow over an exponentially stretching sheet with thermal convective and mass flux conditions: HAM solution

https://doi.org/10.1515/ntrev-2023-0220
received September 24, 2023; accepted February 22, 2024

Abstract: The boundary-layer flow on a shrinking/contracting sheet has abundant industrial applications, which include continuous glass casting, metal or polymer extrusions, and wire drawing. In this regard, the present analysis focuses the hybrid nanofluid flow on an exponentially extending sheet. The water-based hybrid nanofluid flow contains $CoFe_2O_4$ and TiO_2 nanoparticles. Heat transfer rate analysis involves the utilization of the Cattaneo–Christov heat flux model. Moreover, the Brownian motion and thermophoresis effects are used in this novel work. The mathematical model is presented in the form of system of partial differential equations, which is then transformed into system of ordinary differential equations (ODEs) using the similarity variables. The system of ODEs is evaluated by homotopy analysis method. The variation in the flow profiles has been investigated using figures and tables. The conclusions demonstrate that the effect of magnetic parameter is 52% better for hybrid nanofluid flow than for the pure water. Conversely, the increasing magnetic parameter diminishes the thermal transfer rates for water, TiO_2–H_2O, $CoFe_2O_4$–H_2O, and TiO_2–$CoFe_2O_4$/H_2O. The increasing thermophoresis parameter upsurges the thermal flow rate of nanofluids and hybrid nanofluid, while the increasing Brownian motion parameter lessens the thermal transfer rates of nanofluids and hybrid nanofluid. The increasing effect of thermophoresis parameter is 39% better for hybrid nanofluid than for the base fluid. However, the declining impression of Brownian motion factor is 48% greater for hybrid nanofluid related to pure water.

Keywords: hybrid nanofluid flow, nanoparticles, three-dimensional, exponentially stretching sheet, thermal and mass flux conditions, Cattaneo–Christov heat flux model

*** Corresponding author: Gabriella Bognár,** Institute of Machine and Product Design, University of Miskolc, Miskolc-Egyetemváros 3515, Hungary, e-mail: gabriella.v.bognar@uni-miskolc.hu
Showkat Ahmad Lone: Department of Basic Sciences, College of Science and Theoretical Studies, Saudi Electronic University, (Jeddah-M), Riyadh 11673, Saudi Arabia
Zehba Raizah: Department of Mathematics, College of Science, King Khalid University, Abha, Saudi Arabia
Anwar Saeed: Department of Mathematics, Abdul Wali Khan University, Mardan, 23200, Khyber Pakhtunkhwa, Pakistan

Nomenclature

A	temperature exponent parameter
B	concentration exponent parameter
B_0	magnetic field strength (kg s^{-1} A^{-1})
Bi_T	thermal Biot number
C	concentration (mol m^{-3})
C_p	specific heat (J kg^{-1} K^{-1})
D_B	coefficient of Brownian diffusion (m^2 s^{-1})
D_T	coefficient of thermophoresis diffusion (m^2 s^{-1})
Ec	Eckert number
$f_0, g_0, \theta_0, \phi_0$	initial guesses (−)
h_f	coefficient of heat transfer (W m^{-2} K^{-1})
k	thermal conductivity (W m^{-1} K^{-1})
L	reference length (m)
$L_f, L_g, L_\theta, L_\phi$	linear operator (−)
M	magnetic parameter
$m_i (i = 1, 2, 3, \ldots, 10)$	constants in general solution (−)
Nb, Nt	Brownian motion and thermophoresis factors
Sc, Pr	Schmidt and Prandtl numbers
w_1, w_2, w_3	velocity components (m s^{-1})
x, y, z	coordinate axes (m)

Greek letters

ρ	density (kg m^{-3})

μ	dynamic viscosity (kg m^{-1} s^{-1})
σ	electrical conductivity (S m^{-1})
φ_1, φ_2	nanoparticles' volume fractions
Λ	thermal relaxation time parameter
α	ratio of rate parameter

Subscripts

∞	free stream
w	surface
f	fluid
nf	nanofluid
hnf	hybrid nanofluid
1, 2	first and second nanoparticles

1 Introduction

As the technology continues advancement, heat transmission has been the most significant procedure. Transportation, thermal power generation, chemical processes, manufacturing, as well as several other applications and sectors requiring heat generation, demand effective thermal performance to obtain the best results. Various analyses have been attempted in recent years to expand the thermal transfer capabilities of the transmitting medium, which is referred to as thermal transmission of fluid. Maxwell [1] was the first one to present the concept of dissolving solid particles that have high thermal conductivity into a base fluid, which was later carried on by Hamilton and Crosser [2] to increase the thermal conductance of fluid. Despite this, numerous defects and restrictions remained, like clotting in the flow field channel. In response to this limitation, a rapid investigation was conducted, resulting in the development of nanofluids. Choi and Eastman [3] manufactured this innovative thermal transference fluid, and it is thought that owing to its unique characteristic, it will be able to avoid coagulation of the flow passage. With the continuous progress of technology, a novel type of thermal transfer fluid called hybrid nanofluid has emerged as advancement over traditional nanofluids. This innovative fluid is formulated by dispersing two types of particles (nanosized) with excellent thermal conductivity. Sarkar *et al.* [4] highlighted the dominance of hybrid nanofluid regarding their thermophysical properties, heat transmission and potential applications, and obstacles. According to the review, the appropriate hybridization of hybrid nanofluids might make them highly promising for heat transfer augmentation. Nabil *et al.* [5] offered a review article on the hybrid nanofluid flow. Sajid and Ali [6] presented a comprehensive review based on artificial neural networking, experimental and numerical studies of hybrid nanofluids. Devi and Devi [7] investigated the magnetized Cu-Al_2O_3/water hybrid nanofluid flow on elongating surface. Their results signified that the thermal transference rate of the Cu-Al_2O_3/water is better than that of the Cu/water. Zainal *et al.* [8] discussed hybrid nanoparticles' flow containing Cu and Al_2O_3 nanoparticles. For the general synchronism of the electric and magnetic fields, they found that the magnetic field and suction slow down fluid movement. Furthermore, increases in the radiative heat parameter enhances the Nusselt number. Roy and Pop [9] inspected hybrid nanofluid flow over an extending sheet and showed that for the escalating values of magnetic, suction, Cu nanoparticles' volume fraction, and second-grade parameters, the dual solutions' existence region expands. Furthermore, stability analysis is conducted to identify the problem that has actually stable and unstable solutions. Sreedevi and Reddy [10] discussed Williamson hybrid nanoparticles' fluid flow on a gyrating cylinder using the impacts of microorganisms and thermal as well as mass flux model suggested by Cattaneo-Christov. Babu *et al.* [11] investigated computationally the optimization of entropy for MHD nanofluid flow on a nonlinear elongating surface convective and slip constraints at the boundaries and have noted that nonlinear elongating features of the surface are supporting the thermal flow more effectively. Reddy and Sreedevi [12] examined the impacts of thermal as well as mass flux model suggested by Cattaneo–Christov on Maxwell hybrid nanofluid flow on a shrinking/elongating surface. Reddy and Sreedevi [13] explored thermal transportation for carbon nanotubes (CNTs) nanofluid flow in conduit using improved Fourier thermal flux. Harish Babu *et al.* [14] inspected influences and the impacts of inclined magnetic field for CNTs on exponentially elongating sheet using slip effects. Harish Babu *et al.* [15] discussed the collective influences of thermal flow and magnetic field on nanofluid flow over elastic surface. Further research on similar concept is based on previous studies [16–21].

The boundary-layer flow past a shrinking/elongating sheet has numerous applications toward manufacturing processes in the field of engineering, which include continuous glass casting, metal or polymer extrusions, and wire drawing. Crane [22] was the pioneer to investigate flow past a linearly extending sheet. Various flows over a stretched sheet and flows over a contracting surface have just recently been a focus of concern. Bhattacharyya [23] carried out the investigation that indicates the criteria for the presence of steady boundary-layer flow as a result of the exponential shrinking sheet. Their result showed that when the mass suction factor surpasses a specific critical value, steady flow is feasible. Mat Yuzut [24] investigated the heat transmission of MHD fluid flow on exponentially

stretched surface. Their consequences showed that the transmission rate of heat was observed to be declined when the penetrability parameters were increased. Waini *et al.* [25] addressed the hybrid nanofluid flow on an extending/shrinking sheet. It was perceived that the heat transmission rate is augmented with the augmenting volume fraction of the nanoparticles. Further research on hybrid nanofluid flow on an extending/shrinking surfaces can be observed in the study by Ishak [26]. Abbas *et al.* [27] discussed computationally nonlinearly radiative MHD nanofluid flow on a vertical sheet and have noted that skin friction has augmented, while Nusselt number has weakened with expansion in concentration of nanoparticles. Abbas *et al.* [28] examined theoretically nanofluid flow on exponentially elongating surface with impacts of velocity at free stream. Abbas and Shatanawi [29] examined thermal and mass transportations for Casson nanofluid flow on a variable elongating Riga surface and have noted that velocity characteristics weakened with upsurge in micro-polar factor.

Heat and mass transfer is a major topic of research for its applications toward industries and engineering, such as food processing, biomedical sciences, business, and tissue conduction. Akbar *et al.* [30] discussed mixed convective and time-independent flow of a viscous fluid past an extending sheet with magnetic field impact. Their results showed that the augmenting species and thermal Grashof numbers have direct impact on thermal transference rate, while the thermophoresis and Schmidt number have reducing impact of heat transfer rate. Khan *et al.* [31] examined the squeezing flow over a sensor sheet. The results disclosed that growth in squeezing factor has improved the velocity panel of the non-Newtonian fluid. Sandeep *et al.* [32] examined the heat transmission of magnetohydrodynamic (MHD)-radiated flow of a dusty nanofluid containing Cu and CuO nanoparticles on an exponentially extending surface and have noted that thermal flow rate has augmented with escalation in nanoparticles' volume fractions, while the wall fraction has reduced with augmenting nanoparticles' volume fractions. Haq *et al.* [33] discussed the MHD flow of a thermally convective nanofluid past an exponentially expending surface with suction/injection effects. Heat and mass transference of the hybrid nanofluids flow toward different physical phenomena can be analyzed in previous studies [34–41].

The analysis of hybrid nanofluid flow past an exponentially extending sheet has many applications in various fields, especially in engineering, fluid dynamics, and heat transfer. Some of the these applications include heat exchangers, cooling systems, renewable energy systems, material processing, biomedical applications, aerospace engineering, oil and gas industries, and energy conversion systems. Keeping these applications in mind, the current analysis focuses on the flow of hybrid nanofluids over an exponentially extended surface with thermal convection and mass flux constraints. The aim of this analysis is to investigate the flow of hybrid nanofluids containing TiO_2 and $CoFe_2O_4$ nanoparticles and H_2O as a base fluid under thermal convection and mass flux conditions. Furthermore, the Cattaneo–Christov heat flow model is considered to analyze the heat and mass transfer flow. Furthermore, a strong magnetic field is considered to analyze the magnetized flow of the hybrid nanofluid over an extending sheet. Problem is formulated both physically and mathematically in Section 2. The homotopic solution of the present model is presented in Section 3, and the convergence of the applied technique is presented in Section 4. The physical discussion about the obtained results is presented in Section 5 and concluded in Section 6.

2 Formulation of the problem

Take a three-dimensional viscous flow of $TiO_2-CoFe_2O_4/H_2O$ hybrid nanofluid on an exponentially elongating surface. The surface stretches in x- and y-directions with velocities $W_{1w}(x+y) = W_{10}\exp\left[\frac{x+y}{L}\right]$ and $W_{2w}(x+y) = W_{20}\exp\left[\frac{x+y}{L}\right]$, respectively, where W_{10} and W_{20} are the stretching constants. A magnetic field $B(0, 0, B_0)$ is practiced in normal direction to flow of fluid, where B_0 is the magnetic field strength. Figure 1 shows the physical representation of the flow problem. The temperature and concentration of fluid are represented by T and C. T_w, T_∞, C_w, and C_∞ are the surface and free stream temperatures and concentrations, respectively. The stretching surface is also exposed to thermal convection and mass flux conditions. In order to examine the heat transfer rate, the Cattaneo–Christov heat flux model is used. The consequences of thermophoresis and Brownian motion are also assumed. Using the abovementioned suppositions, the principal equations are given in previous studies [42–44]:

$$\frac{\partial w_1}{\partial x} + \frac{\partial w_2}{\partial y} + \frac{\partial w_3}{\partial z} = 0, \tag{1}$$

$$\rho_{hnf}\left(w_1\frac{\partial w_1}{\partial x} + w_2\frac{\partial w_1}{\partial y} + w_3\frac{\partial w_1}{\partial z}\right) = \mu_{hnf}\frac{\partial w_1^2}{\partial z^2} - \sigma_{hnf}B_0^2 w_1, \tag{2}$$

$$\rho_{hnf}\left(w_1\frac{\partial w_2}{\partial x} + w_2\frac{\partial w_2}{\partial y} + w_3\frac{\partial w_2}{\partial z}\right) = \mu_{hnf}\frac{\partial w_2^2}{\partial z^2} - \sigma_{hnf}B_0^2 w_2, \tag{3}$$

$$\left(w_1\frac{\partial T}{\partial x}+w_2\frac{\partial T}{\partial y}+w_3\frac{\partial T}{\partial z}\right)+\lambda\left[w_1^2\frac{\partial^2 T}{\partial x^2}+w_2^2\frac{\partial^2 T}{\partial y^2}+w_3^2\frac{\partial^2 T}{\partial z^2}+2w_1w_2\frac{\partial^2 T}{\partial x\partial y}+2w_2w_3\frac{\partial^2 T}{\partial y\partial z}+2w_1w_3\frac{\partial^2 T}{\partial x\partial z}+\frac{\partial T}{\partial x}\left(w_1\frac{\partial w_1}{\partial x}+w_2\frac{\partial w_1}{\partial y}+w_3\frac{\partial w_1}{\partial z}\right)+\frac{\partial T}{\partial y}\left(w_1\frac{\partial w_2}{\partial x}+w_2\frac{\partial w_2}{\partial y}+w_3\frac{\partial w_2}{\partial z}\right)+\frac{\partial T}{\partial z}\left(w_1\frac{\partial w_3}{\partial x}+w_2\frac{\partial w_3}{\partial y}+w_3\frac{\partial w_3}{\partial z}\right)\right]=\frac{k_{\mathrm{hnf}}}{(\rho C_{\mathrm{p}})_{\mathrm{hnf}}}\frac{\partial^2 T}{\partial z^2}+\frac{\sigma_{\mathrm{hnf}}}{(\rho C_{\mathrm{p}})_{\mathrm{hnf}}}(w_1^2+w_2^2)+\frac{(\rho C_{\mathrm{p}})_{\mathrm{np}}}{(\rho C_{\mathrm{p}})_{\mathrm{hnf}}}\left[D_{\mathrm{B}}\frac{\partial T}{\partial z}\frac{\partial C}{\partial z}+\frac{D_{\mathrm{T}}}{T_\infty}\left(\frac{\partial T}{\partial z}\right)^2\right], \tag{4}$$

$$\left\{\begin{aligned}&\frac{\mu_{\mathrm{hnf}}}{\mu_{\mathrm{f}}}=\frac{1}{(1-\varphi_{1,2})^{2.5}},\quad \frac{\rho_{\mathrm{hnf}}}{\rho_{\mathrm{f}}}=(1-\varphi_{1,2})+\frac{\rho_{1,2}\varphi_{1,2}}{\rho_{\mathrm{f}}},\\&\frac{(\rho C_{\mathrm{p}})_{\mathrm{hnf}}}{(\rho C_{\mathrm{p}})_{\mathrm{f}}}=(1-\varphi_{1,2})+\frac{(\rho C_{\mathrm{p}})_{1,2}(\rho C_{\mathrm{p}})_{1,2}}{(\rho C_{\mathrm{p}})_{\mathrm{f}}},\\&\frac{\sigma_{\mathrm{hnf}}}{\sigma_{\mathrm{f}}}=1+\frac{3\left[\left(\frac{\sigma_{1,2}}{\sigma_f}-1\right)\varphi_{1,2}\right]}{\left(\frac{\sigma_{1,2}}{\sigma_{\mathrm{f}}}+2\right)-\left(\frac{\sigma_{1,2}}{\sigma_{\mathrm{f}}}-1\right)\varphi_{1,2}},\\&\frac{k_{\mathrm{hnf}}}{k_{\mathrm{f}}}=1+\frac{3\left[\left(\frac{k_{1,2}}{k_{\mathrm{f}}}-1\right)\varphi_{1,2}\right]}{\left(\frac{k_{1,2}}{k_{\mathrm{f}}}+2\right)-\left(\frac{k_{1,2}}{k_{\mathrm{f}}}-1\right)\varphi_{1,2}}.\end{aligned}\right\} \tag{7}$$

$$\left\{\begin{aligned}&\frac{\mu_{\mathrm{hnf}}}{\mu_{\mathrm{f}}}=\frac{1}{(1-\varphi_1-\varphi_2)^{2.5}},\quad \frac{\rho_{\mathrm{hnf}}}{\rho_{\mathrm{f}}}=(1-\varphi_2)\left[(1-\varphi_1)+\frac{\rho_1\varphi_1}{\rho_{\mathrm{f}}}\right]+\frac{\rho_2\varphi_2}{\rho_{\mathrm{f}}}\\&\frac{(\rho C_{\mathrm{p}})_{\mathrm{hnf}}}{(\rho C_{\mathrm{p}})_{\mathrm{f}}}=(1-\varphi_2)\left[(1-\varphi_1)+\frac{(\rho C_{\mathrm{p}})_1\varphi_1}{(\rho C_{\mathrm{p}})_{\mathrm{f}}}\right]+\frac{(\rho C_{\mathrm{p}})_2\varphi_2}{(\rho C_{\mathrm{p}})_{\mathrm{f}}},\\&\frac{\sigma_{\mathrm{hnf}}}{\sigma_{\mathrm{f}}}=1+\frac{3(\varphi_1+\varphi_2)[\varphi_1\sigma_1+\varphi_2\sigma_2-\sigma_f(\varphi_1+\varphi_2)]}{\varphi_1\sigma_1+\varphi_2\sigma_2+2\sigma_{\mathrm{f}}(\varphi_1+\varphi_2)-\sigma_{\mathrm{f}}(\varphi_1+\varphi_2)\left[\begin{matrix}\varphi_1\sigma_1+\varphi_2\sigma_2\\-\sigma_{\mathrm{f}}(\varphi_1+\varphi_2)\end{matrix}\right]},\\&\frac{k_{\mathrm{hnf}}}{k_{\mathrm{f}}}=1+\frac{3(\varphi_1+\varphi_2)[\varphi_1k_1+\varphi_2k_2-k_{\mathrm{f}}(\varphi_1+\varphi_2)]}{\varphi_1k_1+\varphi_2k_2+2k_{\mathrm{f}}(\varphi_1+\varphi_2)-k_{\mathrm{f}}(\varphi_1+\varphi_2)\left[\begin{matrix}\varphi_1k_1+\varphi_2k_2\\-k_{\mathrm{f}}(\varphi_1+\varphi_2)\end{matrix}\right]}.\end{aligned}\right\} \tag{8}$$

$$w_1\frac{\partial C}{\partial x}+w_2\frac{\partial C}{\partial y}+w_3\frac{\partial C}{\partial z}=\frac{D_{\mathrm{T}}}{T_\infty}\frac{\partial^2 T}{\partial z^2}+D_{\mathrm{B}}\frac{\partial^2 C}{\partial z^2}, \tag{5}$$

with boundary conditions [42–44]:

$$\left.\begin{aligned}&w_1=W_{1\mathrm{w}}(x+y)=W_{10}\exp\left[\frac{x+y}{L}\right],\\&w_2=W_{2\mathrm{w}}(x+y)=W_{20}\exp\left[\frac{x+y}{L}\right],\\&w_3=0,\ k_{\mathrm{hnf}}\frac{\partial T}{\partial z}=-h_{\mathrm{f}}(T_{\mathrm{f}}-T),\\&\frac{D_{\mathrm{T}}}{T_\infty}\frac{\partial T}{\partial z}+D_{\mathrm{B}}\frac{\partial C}{\partial z}=0,\end{aligned}\right\}\ \text{at } z=0, \tag{6}$$

$$w_1\to 0,\quad w_2\to 0,\quad T\to T_\infty,\quad C\to C_\infty,\}\ \text{as } z\to\infty.$$

The thermophysical characteristics of the nanofluid and hybrid nanofluid, respectively, are described as follows with their numerical values depicted in Table 1:

The following similarity transformations are according to flow assumptions:

$$\left\{\begin{aligned}&\eta=\sqrt{\frac{W_{10}}{2\nu_{\mathrm{f}}L}}\exp\left[\frac{x+y}{2L}\right]z,\\&w_1=W_{10}\exp\left[\frac{x+y}{L}\right]f'(\eta),\\&w_2=W_{20}\exp\left[\frac{x+y}{L}\right]g'(\eta),\\&w_3=\sqrt{\frac{\nu_{\mathrm{f}}W_{10}}{2L}}\exp\left[\frac{x+y}{2L}\right]\{f(\eta)+g(\eta)+\eta(f'(\eta)+g'(\eta))\},\\&T=T_\infty+T_0\exp\left[\frac{A(x+y)}{2L}\right]\theta(\eta),\\&C=C_\infty+C_0\exp\left[\frac{B(x+y)}{2L}\right]\phi(\eta).\end{aligned}\right\} \tag{9}$$

By employing equation (9) in the leading equations (1)–(4), we have

$$\left\{\left\{\frac{1}{(1-\varphi_1-\varphi_2)^{2.5}}\right\}f''' + \left\{(1-\varphi_2)\left[(1-\varphi_1)+\frac{\rho_1\varphi_2}{\rho_f}\right]+\frac{\rho_2\varphi_2}{\rho_f}\right\}\begin{bmatrix} f''\{f+g\}- \\ 2f'\{f'+g'\}\end{bmatrix}\right\} - \left\{1+\frac{3(\varphi_1+\varphi_2)[\varphi_1\sigma_2+\varphi_1\sigma_2-\sigma_f(\varphi_1+\varphi_2)]}{\varphi_1\sigma_1+\varphi_2\sigma_2+2\sigma_f(\varphi_1+\varphi_2)-\sigma_f(\varphi_1+\varphi_2)\begin{bmatrix}\varphi_1\sigma_1+\varphi_2\sigma_2 \\ -\sigma_f(\varphi_1+\varphi_2)\end{bmatrix}}\right\}M^2f'\right\} = 0, \tag{10}$$

$$\left\{\left\{\frac{1}{(1-\varphi_1-\varphi_2)^{2.5}}\right\}g''' + \left\{(1-\varphi_2)\left[(1-\varphi_1)+\frac{\rho_1\varphi_2}{\rho_f}\right]+\frac{\rho_2\varphi_2}{\rho_f}\right\}\begin{bmatrix} g''\{f+g\}- \\ 2g'\{f'+g'\}\end{bmatrix}\right\} - \left\{1+\frac{3(\varphi_1+\varphi_2)[\varphi_1\sigma_2+\varphi_1\sigma_2-\sigma_f(\varphi_1+\varphi_2)]}{\varphi_1\sigma_1+\varphi_2\sigma_2+2\sigma_f(\varphi_1+\varphi_2)-\sigma_f(\varphi_1+\varphi_2)\begin{bmatrix}\varphi_1\sigma_1+\varphi_2\sigma_2 \\ -\sigma_f(\varphi_1+\varphi_2)\end{bmatrix}}\right\}M^2g'\right\} = 0, \tag{11}$$

$$\left\{\frac{\left\{1+\frac{3(\varphi_1+\varphi_1)[\varphi_1k_1+\varphi_2k_2-k_f(\varphi_1+\varphi_2)]}{\varphi_1k_1+\varphi_2k_2+2k_f(\varphi_1+\varphi_2)-k_f(\varphi_1+\varphi_2)\begin{bmatrix}\varphi_1k_1+\varphi_2k_2 \\ -k_f(\varphi_1+\varphi_2)\end{bmatrix}}\right\}}{\left\{(1-\varphi_2)\left[(1-\varphi_1)+\frac{(\rho C_p)_1\varphi_1}{(\rho C_p)_f}\right]+\frac{(\rho C_p)_2\varphi_2}{(\rho C_p)_f}\right\}}\frac{1}{Pr}\theta'' + \left(Nb\theta'\phi'+\frac{Nt}{Nb}\theta''\right) - A\theta\{f'+g'\}+A\theta'\{f+g\} + \frac{\Lambda}{2}\begin{bmatrix}\{\xi(f'+g')+(1+2A)(f+g)\}(f'+g')\theta' - A\begin{Bmatrix}(A+2) \\ (f'+g')^2\end{Bmatrix} \\ -(f''+g'')(f+g)\theta-(f+g)^2\theta''\end{bmatrix} - \frac{\left\{1+\frac{3(\varphi_1+\varphi_2)[\varphi_1\sigma_2+\varphi_1\sigma_2-\sigma_f(\varphi_1+\varphi_2)]}{\varphi_1\sigma_1+\varphi_2\sigma_2+2\sigma_f\begin{pmatrix}\varphi_1+ \\ \varphi_2\end{pmatrix}-\sigma_f\begin{pmatrix}\varphi_1+ \\ \varphi_2\end{pmatrix}\begin{bmatrix}\varphi_1\sigma_1+\varphi_2\sigma_2- \\ \sigma_f(\varphi_1+\varphi_2)\end{bmatrix}}\right\}}{\left\{(1-\varphi_2)\left[(1-\varphi_1)+\frac{(\rho C_p)_1\varphi_1}{(\rho C_p)_f}\right]+\frac{(\rho C_p)_2\varphi_2}{(\rho C_p)_f}\right\}}M^2Ec\{f'^2+g'^2\}\right\} = 0, \tag{12}$$

$$\phi'' - ScB(f'+g')\phi + Sc(f+g)\phi' + \frac{Nt}{Nb}\theta'' = 0, \tag{13}$$

$$\begin{bmatrix} f(0)=0,\ f'(0)=1,\ f'(\infty)=0, \\ g(0)=0,\ g'(0)=\alpha,\ g'(\infty)=0, \\ \frac{k_{hnf}}{k_f}\theta'(0) = -Bi_T(\theta(0)-1),\ \theta(\infty)=0, \\ Nb\phi'(0)+Nt\theta'(0)=0,\ \phi(\infty)=0.\end{bmatrix} \tag{14}$$

The dimensionless factors are defined as

$$\begin{bmatrix} M^2=\frac{2\sigma_fLB_0^2}{W_{1w}\rho_f}, \quad Pr=\frac{\mu_f(\rho C_p)_f}{k_f}, \\ Ec=\frac{W_{1w}^2}{C_p(T_w-T_\infty)}, \quad Nb=\frac{(\rho C_p)_{np}}{(\rho C_p)_f}\frac{D_B(C_w-C_\infty)}{\nu_f}, \\ Nt=\frac{(\rho C_p)_{np}}{(\rho C_p)_f}\frac{D_T(T_w-T_\infty)}{\nu_fT_\infty}, \quad Sc=\frac{\nu_f}{D_B}, \\ \alpha=\frac{W_{20}}{W_{10}}, \quad \Lambda=\frac{\lambda W_{1w}}{L}, \quad Bi_T=\gamma=\frac{h_f}{k_f}\sqrt{\frac{2\nu_fL}{W_{1w}}}.\end{bmatrix} \tag{15}$$

The skin friction coefficients along primary and secondary directions are illustrated as:

$$\left.\begin{aligned} C_{fx} &= \frac{\tau_{wx}}{\frac{1}{2}\rho_f w_1^2}, \quad \text{where} \quad \tau_{wx} = \mu_{hnf}\frac{\partial w_1}{\partial z}\Big|_{z=0}, \\ C_{fy} &= \frac{\tau_{wy}}{\frac{1}{2}\rho_f w_2^2}, \quad \text{where} \quad \tau_{wy} = \mu_{hnf}\frac{\partial w_2}{\partial z}\Big|_{z=0}. \end{aligned}\right\} \tag{16}$$

The dimensionless forms are written as

$$\left.\begin{aligned} \sqrt{\frac{\mathrm{Re}_x}{2}}\exp\left[\frac{-3(x+y)}{2L}\right]C_{fx} &= \left\{\frac{1}{(1-\varphi_1-\varphi_2)^{2.5}}\right\}f''(0), \\ \sqrt{\frac{\mathrm{Re}_x}{2}}\exp\left[\frac{-3(x+y)}{2L}\right]C_{fy} &= \left\{\frac{1}{(1-\varphi_1-\varphi_2)^{2.5}}\right\}g''(0), \end{aligned}\right\} \tag{17}$$

Or

$$\left.\begin{aligned} C_x &= \left\{\frac{1}{(1-\varphi_1-\varphi_2)^{2.5}}\right\}f''(0), \\ C_y &= \left\{\frac{1}{(1-\varphi_1-\varphi_2)^{2.5}}\right\}g''(0), \end{aligned}\right\} \tag{18}$$

where $C_x = \sqrt{\frac{\mathrm{Re}_x}{2}}\exp\left[\frac{-3(x+y)}{2L}\right]C_{fx}$ and $C_y = \sqrt{\frac{\mathrm{Re}_x}{2}}\exp\left[\frac{-3(x+y)}{2L}\right]C_{fy}$. Also, $\mathrm{Re}_x = \frac{w_{1w}L}{\nu_f}$ and $\mathrm{Re}_y = \frac{w_{2w}L}{\nu_f}$ are the local Reynolds numbers.

The local Nusselt number is described as

$$\mathrm{Nu}_x = \frac{xq_w}{k_f(T_w - T_\infty)}, \quad \text{where} \quad q_w = -k_{hnf}\frac{\partial T}{\partial z}\Big|_{z=0}. \tag{19}$$

In dimensionless form, we can write

$$\frac{\sqrt{2}L}{x}\exp\left[\frac{-(x+y)}{2L}\right]\frac{\mathrm{Nu}_x}{\sqrt{\mathrm{Re}_x}} = -\left\{1 + \frac{3(\varphi_1+\varphi_1)[\varphi_1k_1 + \varphi_2k_2 - k_f(\varphi_1+\varphi_2)]}{\varphi_1k_1 + \varphi_2k_2 + 2k_f(\varphi_1+\varphi_2) - k_f(\varphi_1+\varphi_2)\begin{bmatrix}\varphi_1k_1+\varphi_2k_2\\ -k_f(\varphi_1+\varphi_2)\end{bmatrix}}\right\}\theta'(0). \tag{20}$$

Or

$$\mathrm{Nu} = -\left\{1 + \frac{3(\varphi_1+\varphi_2)[\varphi_1k_1 + \varphi_2k_2 - k_f(\varphi_1+\varphi_2)]}{\varphi_1k_1 + \varphi_2k_2 + 2k_f(\varphi_1+\varphi_2) - k_f(\varphi_1+\varphi_2)\begin{bmatrix}\varphi_1k_1+\varphi_2k_2\\ -k_f(\varphi_1+\varphi_2)\end{bmatrix}}\right\}\theta'(0). \tag{21}$$

where $\mathrm{Nu} = \frac{\sqrt{2}L}{x}\exp\left[\frac{-(x+y)}{2L}\right]\frac{\mathrm{Nu}_x}{\sqrt{\mathrm{Re}_x}}$.

The Sherwood number is defined as

$$\mathrm{Sh}_x = \frac{xq_m}{D_B(C_w - C_\infty)}, \quad \text{where} \quad q_m = -D_B\frac{\partial C}{\partial z}\Big|_{z=0}. \tag{22}$$

In dimensionless form, we can write

$$\frac{\sqrt{2}L}{x}\exp\left[\frac{-(x+y)}{2L}\right]\frac{\mathrm{Sh}_x}{\sqrt{\mathrm{Re}_x}} = -\phi'(0). \tag{23}$$

Or

$$\mathrm{Sh} = -\phi'(0). \tag{24}$$

where $\mathrm{Sh} = \frac{\sqrt{2}L}{x}\exp\left[\frac{-(x+y)}{2L}\right]\frac{\mathrm{Sh}_x}{\sqrt{\mathrm{Re}_x}}$.

3 Homotopy analysis method (HAM) solution

The HAM is the method used in this work to determine the solutions. The initial guesses and linear operators are defined as follows:

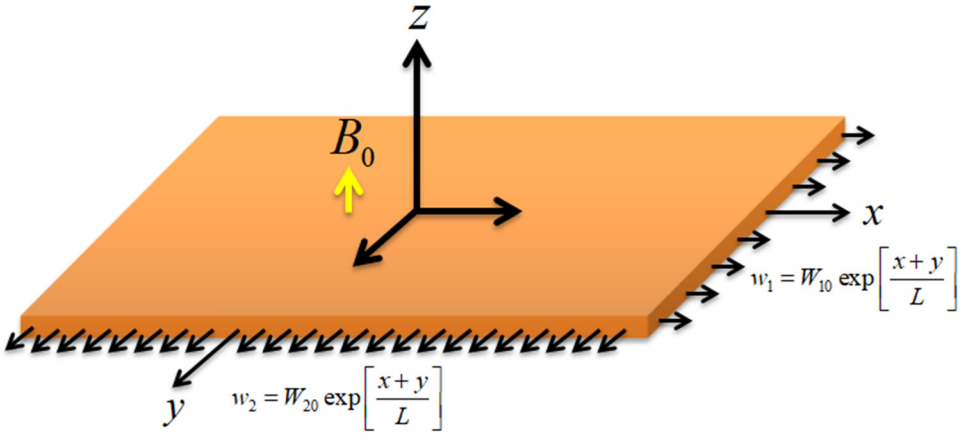

Figure 1: Geometrical view of flow problem.

Table 1: Thermophysical features of the nanoparticles and pure fluid [45–48]

Base fluid/nanoparticles	C_p	ρ	k	σ
H_2O	4,179	997.1	0.6071	5.5×10^{-6}
TiO_2	686.2	4,250	8.9538	2.38×10^{6}
$CoFe_2O_4$	700	4,907	3.7	5.51×10^{9}

$$\left.\begin{aligned} f_0(\xi) &= 1 - e^{-\xi}, \\ g_0(\xi) &= \alpha(1 - e^{-\xi}), \\ \theta_0(\xi) &= \left(\frac{k_{\mathrm{hnf}}}{k_{\mathrm{f}}}\frac{\mathrm{Bi_T}}{1 + \mathrm{Bi_T}}\right)e^{-\xi}, \\ \phi_0(\xi) &= -\left(\frac{\mathrm{Nt}}{\mathrm{Nb}}\frac{\mathrm{Bi_T}}{1 + \mathrm{Bi_T}}\right)e^{-\xi}. \end{aligned}\right\} \tag{25}$$

$$\left.\begin{aligned} L_f(f) &= f''' - f', \\ L_g(g) &= g''' - g', \\ L_\theta(\theta) &= \theta'' - \theta, \\ L_\phi(\phi) &= \phi'' - \phi, \end{aligned}\right\} \tag{26}$$

with properties:

$$\left.\begin{aligned} L_f(\ell_1 + \ell_2 e^{-\xi} + \ell_3 e^{\xi}) &= 0, \\ L_g(\ell_4 + \ell_5 e^{-\xi} + \ell_6 e^{\xi}) &= 0, \\ L_\theta(\ell_7 e^{-\xi} + \ell_8 e^{\xi}) &= 0, \\ L_\phi(\ell_9 e^{-\xi} + \ell_{10} e^{\xi}) &= 0. \end{aligned}\right\} \tag{27}$$

Here $\ell_i (i = 1, 2, 3, \ldots, 10)$ are the constants in general solution.

Table 2: Comparison of the present results of $\theta'(0)$ with formerly reported outcomes, when $\varphi_1 = \varphi_2 = 0.0$

Pr	A	Liu *et al.* [49]	Magyari and Keller *et al.* [50]	Ramzan *et al.* [51]	Present results
1	−1.5	0.37741256	0.377413	0.37741301	0.37714
	0	−0.54964375	−0.549643	−0.54964339	−0.54964
	1	−0.95478270	−0.954782	−0.95478277	−0.95478
	3	−1.56029540	−1.560294	−1.56029499	−1.56029
5	−1.5	1.35324050	1.353240	1.35324055	1.35324
	0	−1.52123900	−1.521243	−1.52123893	−1.52123
	1	−2.50013157	−2.500135	−2.500135210	−2.50014
	3	−3.88655510	−3.886555	−3.88655512	−3.88656
10	−1.5	−2.20002816	2.200000	2.20000798	2.20008
	0	−2.25742372	−2.2574249	−2.25742910	−2.25743
	1	−3.66037218	−3.660379	−3.66037911	−3.66038
	3	−5.62819631	−5.635369	−5.635316812	−5.63532

Table 3: Impact of M on C_x

$\phi_1 = \phi_2$	M	TiO_2–H_2O	$CoFe_2O_4$–H_2O	TiO_2–$CoFe_2O_4$/H_2O
0.0	0.5	1.52250	1.52250	1.52250
0.0	1.0	1.70583	1.70583	1.70583
0.0	1.5	1.88917	1.88917	1.88917
0.05	0.5	1.83757	1.86401	2.23569
0.05	1.0	2.07889	2.10533	2.55160
0.05	1.5	2.32022	2.34665	2.86751

4 HAM convergence

In order to investigate the convergence of series solutions, HAM is applied. The liner auxiliary factors $\hbar_f, \hbar_g, \hbar_\theta$, and $\hbar_\phi$ play a main role in regulating and adjusting the convergence areas of the modeled equations. Thus, the $\hbar$-curves for velocities, thermal, and concentration distributions are plotted in Figure 2. It can be understood from Figure 2 that these flow profiles converge in their respective regions.

5 Results and discussion

This segment deals the variations in velocities along x- and y-axes ($f'(\xi)$, $g'(\xi)$), temperature ($\theta(\xi)$), and concentration ($\phi(\xi)$) profiles *via* different physical parameters, which are displayed in Tables 3–5 and Figures 3–13. The ranges of the embedded factor are chosen as $M = 0.4$, Pr = 6.2, Ec = 0.2, Nb = 0.1, Nt = 0.1, Sc = 0.3, $\alpha = 1.0$, $\Lambda = 0.5$, $A = 0.2$, $B = 0.2$, $\varphi_1 = 0.04$, $\varphi_2 = 0.04$, and $\mathrm{Bi_T} = 0.5$. Table 2 shows the assessment of the current consequences with previously issued reports and observed a strong promise with those published reports. Table 3 portrays the impact of M on skin friction along x-direction for water, $TiO_2 - H_2O$, $CoFe_2O_4 - H_2O$, and $TiO_2 - CoFe_2O_4/H_2O$. It is found that the increase in M boosts the skin friction. Physically, growth in M augments Lorentz force that opposes velocity and hence the skin friction coefficients augment. Additionally, the effect of magnetic parameter is lower on pure water as compared to nanofluids and hybrid nanofluid. This is for mixing of solid nanoparticles in water,

Table 4: Impact of M on C_y

$\phi_1 = \phi_2$	M	TiO_2–H_2O	$CoFe_2O_4$–H_2O	TiO_2–$CoFe_2O_4$/H_2O
0.0	0.5	0.15225	0.15225	0.15225
0.0	1.0	0.17058	0.17058	0.17058
0.0	1.5	0.18891	0.18891	0.18891
0.05	0.5	0.18375	0.18640	0.22356
0.05	1.0	0.20788	0.21053	0.25516
0.05	1.5	0.23202	0.23466	0.28675

Table 5: Impacts of M, Nt and Nb on Nu

$\phi_1 = \phi_2$	M	Nt	Nb	TiO_2–H_2O	$CoFe_2O_4$–H_2O	TiO_2–$CoFe_2O_4$/H_2O
0.0	0.5	0.3	0.3	0.05032	0.05032	0.05032
0.0	1.0			0.05400	0.05400	0.05400
0.0	1.5			0.06022	0.06022	0.06022
0.0		0.4		0.08066	0.08066	0.08066
0.0		0.6		0.08302	0.08302	0.08302
0.0		0.8		0.08424	0.08424	0.08424
0.0			0.4	0.07532	0.07532	0.07532
0.0			0.6	0.06926	0.06926	0.06926
0.0			0.8	0.06320	0.06320	0.06320
0.05	0.5	0.3	0.3	0.05916	0.05758	0.11552
0.05	1.0			0.06056	0.05921	0.11593
0.05	1.5			0.06139	0.06019	0.11686
0.05		0.4		0.08027	0.04673	0.11244
0.05		0.6		0.08294	0.04933	0.11304
0.05		0.8		0.08433	0.05067	0.11335
0.05			0.4	0.07424	0.04087	0.11111
0.05			0.6	0.06740	0.03422	0.10960
0.05			0.8	0.06056	0.02757	0.10809

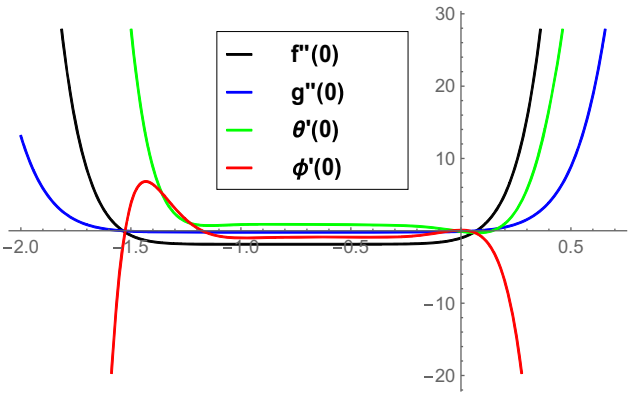

Figure 2: $\hbar$-curves for $f''(0)$, $g''(0)$, $\theta'(0)$, and $\phi'(0)$.

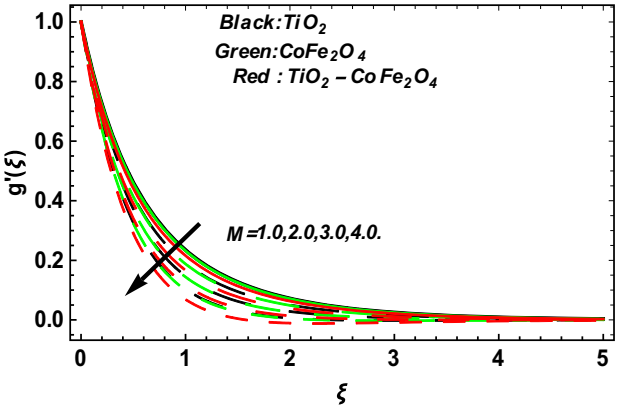

Figure 4: Impact of M on $g'(\xi)$.

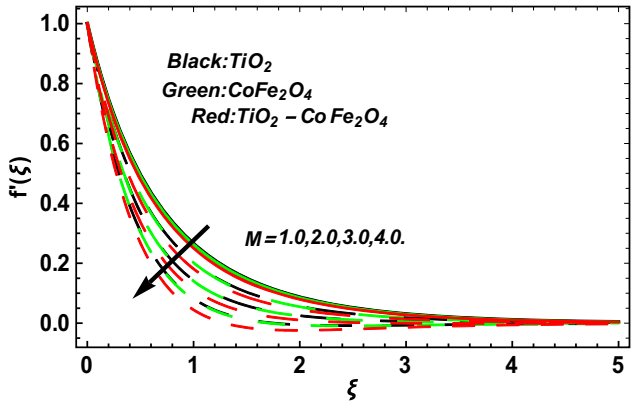

Figure 3: Impact of M on $f'(\xi)$.

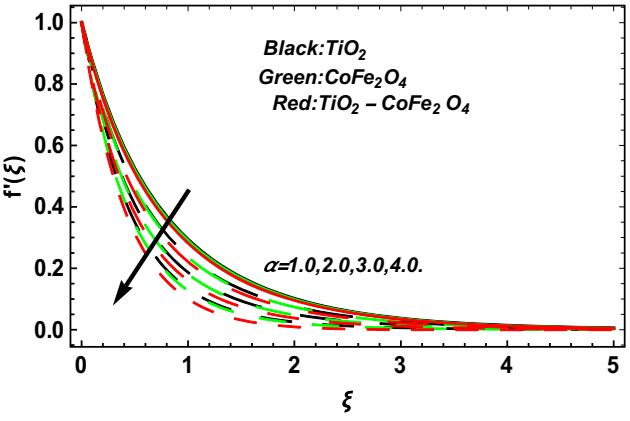

Figure 5: Impact of α on $f'(\xi)$.

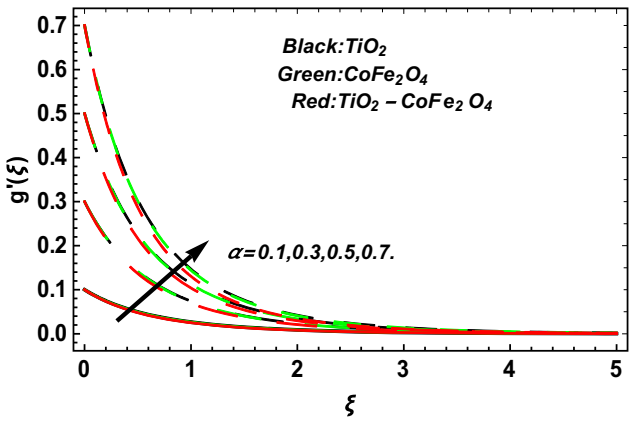

Figure 6: Impact of α on $g'(\xi)$.

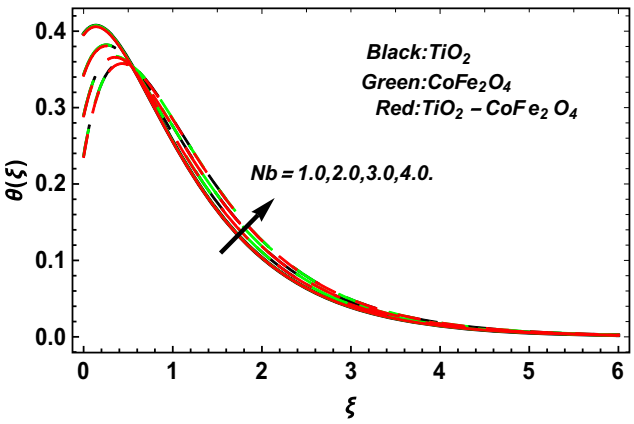

Figure 9: Impact of Nb on $\theta(\xi)$.

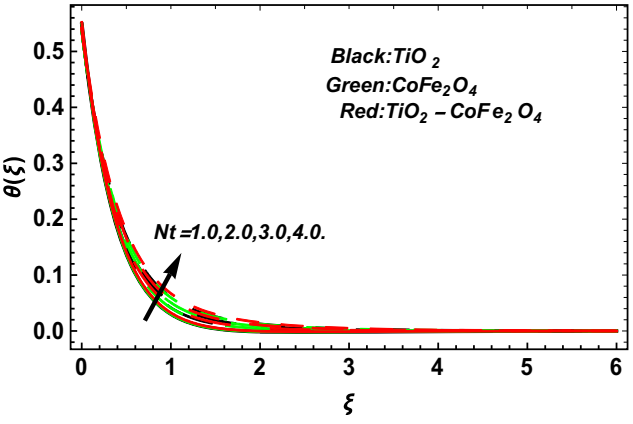

Figure 7: Impact of Nt on $\theta(\xi)$.

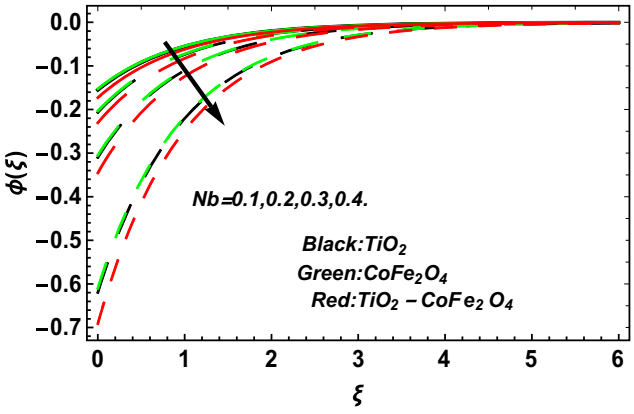

Figure 10: Impact of Nb on $\phi(\xi)$.

which increases the electrical conductance of base fluid, and hence, dominant impacts are found in nanofluids and hybrid nanofluid. Also, this effect is greater for $TiO_2-CoFe_2O_4/H_2O$ than for $CoFe_2O_4-H_2O$ and is greater for $CoFe_2O_4-H_2O$ than for TiO_2-H_2O. Furthermore, the effect of magnetic parameter (M = 1.5) is 52% greater for hybrid nanofluid flow than for the pure water. A similar impression of M is found on skin friction along y-direction for water, TiO_2-H_2O, $CoFe_2O_4-H_2O$, and $TiO_2-CoFe_2O_4/H_2O$, as portrayed in Table 4. Table 5 portrays

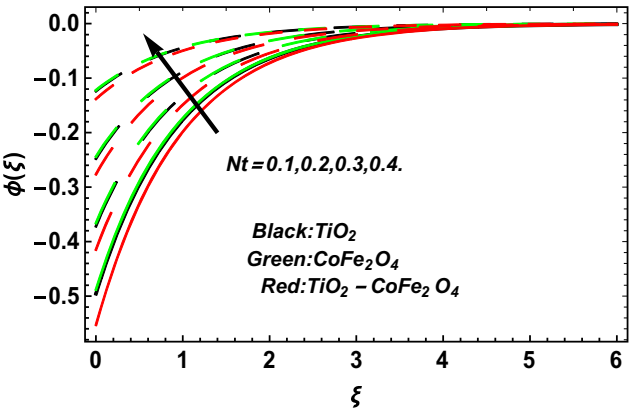

Figure 8: Impact of Nt on $\phi(\xi)$.

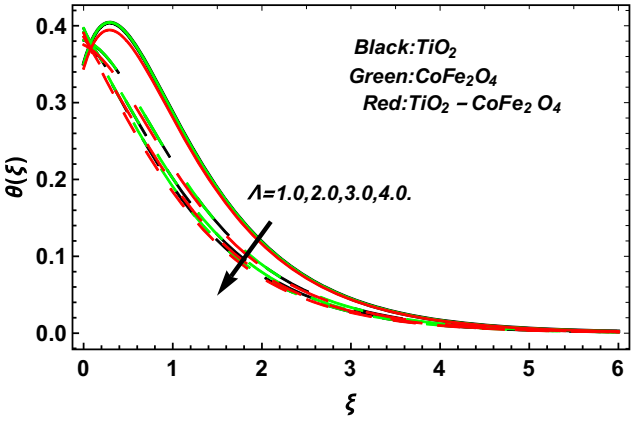

Figure 11: Impact of Λ on $\theta(\xi)$.

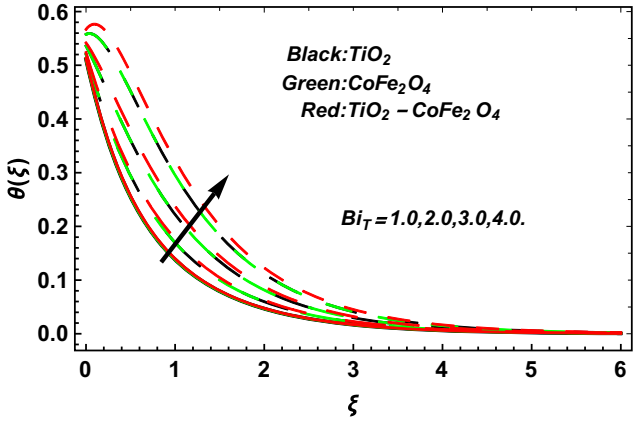

Figure 12: Impact of Bi_T on $\theta(\xi)$.

the influence of various factors on Nusselt number for water, TiO_2-H_2O, $CoFe_2O_4-H_2O$, and $TiO_2-CoFe_2O_4/H_2O$. Growth in M reduces the heat transfer rates of water, TiO_2-H_2O, $CoFe_2O_4-H_2O$, and $TiO_2-CoFe_2O_4/H_2O$. Physically, the upsurge in M hikes the shear stress and causes a growing behavior in skin frictions and Nusselt number. Furthermore, Nusselt number is greater for $TiO_2-CoFe_2O_4/H_2O$, TiO_2-H_2O and $CoFe_2O_4-H_2O$ compared to pure water. Additionally, the greatest increasing behavior is found for $TiO_2-CoFe_2O_4/H_2O$. The increasing thermophoresis parameter increases the heat transfer rates of water, TiO_2-H_2O, $CoFe_2O_4-H_2O$, and $TiO_2-CoFe_2O_4/H_2O$, while the increasing Brownian motion parameter reduces the heat transfer rates of pure water, TiO_2-H_2O, $CoFe_2O_4-H_2O$, and $TiO_2-CoFe_2O_4/H_2O$. The increasing effect of thermophoresis parameter (Nt = 0.4) is 39% higher for hybrid nanofluid than for pure fluid. Conversely, the declining impact of Nb = 0.4 is 48% higher for hybrid nanofluid. Figures 3 and 4 show the impression of M on velocity profiles ($f'(\xi)$, $g'(\xi)$). Growth in M lessens both $f'(\xi)$ and $g'(\xi)$. The increasing M generates the Lorentz force that opposes

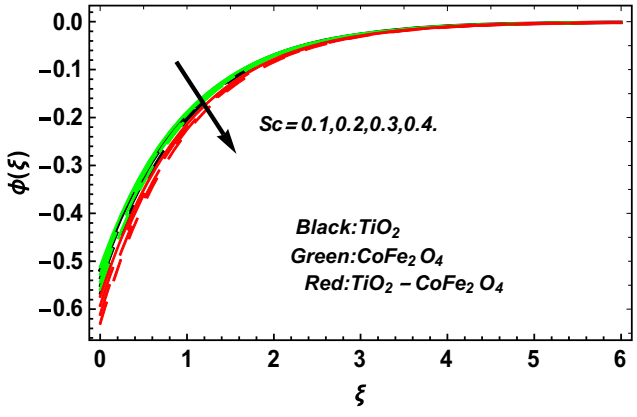

Figure 13: Impact of Sc on $\phi(\xi)$.

the TiO_2-H_2O, $CoFe_2O_4-H_2O$, and $TiO_2-CoFe_2O_4/H_2O$ profiles. This opposing force reduces the velocities profiles, as shown in Figures 3 and 4. Furthermore, the impact of M is greater for hybrid nanofluid flow in contrast of nanofluids. This effect is for greater electrical conductance of the hybrid nanofluid. Figures 5 and 6 demonstrate the impression of α on $f'(\xi)$ and $g'(\xi)$. Growth in α diminishes the velocity profiles of the TiO_2-H_2O, $CoFe_2O_4-H_2O$, and $TiO_2-CoFe_2O_4/H_2O$ along the x-direction, while reduces along the y-direction. The ratio parameter is defined as $\alpha = W_{20}/W_{10}$, which clearly shows that there is a direct relation between the stretching constant W_{20} and α, while an inverse relation between the stretching constant W_{10} and α. Thus, the increasing α has direct relation to W_{20} and reverse relation to W_{10}. Therefore, the velocity profiles of the TiO_2-H_2O, $CoFe_2O_4-H_2O$, and $TiO_2-CoFe_2O_4/H_2O$ along the x-direction reduce and the velocity profiles of the TiO_2-H_2O, $CoFe_2O_4-H_2O$, and $TiO_2-CoFe_2O_4/H_2O$ along the y-direction augment. Figures 7 and 8 depict the impacts of Nt on $\theta(\xi)$ and $\phi(\xi)$ of the TiO_2-H_2O, $CoFe_2O_4-H_2O$, and $TiO_2-CoFe_2O_4/H_2O$. The increasing Nt means the strengthening of thermophoretic force. On surface of the stretching sheet, a higher concentration is witnessed, whereas the concentration reduces as the nanofluids and hybrid nanofluid moves away from the surface. Additionally, the higher impression is observed for both TiO_2-H_2O and $CoFe_2O_4-H_2O$ as compared to $TiO_2-CoFe_2O_4/H_2O$. On the other hand, the impact of Nt is slightly greater for $TiO_2-CoFe_2O_4/H_2O$ as compared to TiO_2-H_2O and $CoFe_2O_4-H_2O$. Figures 9 and 10 depict the effects of Nb on $\theta(\xi)$ and $\phi(\xi)$ of the TiO_2-H_2O, $CoFe_2O_4-H_2O$, and $TiO_2-CoFe_2O_4/H_2O$. Upsurge in Nb boosts $\theta(\xi)$, while it diminishes $\phi(\xi)$. The influence of Nb is better for $TiO_2-CoFe_2O_4/H_2O$ as compared to TiO_2-H_2O and $CoFe_2O_4-H_2O$. Figure 11 illustrates the effects of Λ on $\theta(\xi)$ of the TiO_2-H_2O, $CoFe_2O_4-H_2O$, and $TiO_2-CoFe_2O_4/H_2O$. The increasing Λ reduces the thermal profiles of TiO_2-H_2O, $CoFe_2O_4-H_2O$, and $TiO_2-CoFe_2O_4/H_2O$. The increasing Λ indicates that the nanofluids and hybrid nanofluid take extra time to transfer heat into surrounding particles, which consequently decline the thermal profiles. Additionally, the reducing impact is greater on $TiO_2-CoFe_2O_4/H_2O$ as compared to $CoFe_2O_4-H_2O$ and TiO_2-H_2O. Figure 12 shows the impression of Bi_T on thermal distribution of TiO_2-H_2O, $CoFe_2O_4-H_2O$, and $TiO_2-CoFe_2O_4/H_2O$. The increasing Bi_T escalates the thermal profiles. The increasing values of Bi_T understand the augmentation in convective heating at the surface. It should be noted that the isothermal case is achieved for $Bi_T \to \infty$ and the isoflux wall condition is achieved for $Bi_T = 0$. It is obvious that the increasing Bi_T has greater impact on the surface as revealed in Figure 12. Figure 13 illustrates the impression of Sc on

concentration profiles of the TiO_2-H_2O, $CoFe_2O_4-H_2O$, and $TiO_2-CoFe_2O_4/H_2O$. Growth in Sc diminishes the concentration profiles. Schmidt number is defined as $Sc = \frac{\nu_f}{D_B}$. From here, we see that there is an inverse relation among Schmidt number and Brownian diffusion. So a hike in Schmidt number diminishes the Brownian diffusion of the fluid flow that ultimately diminishes the concentration distribution. Furthermore, the decreasing impact of Sc is dominant for $TiO_2-CoFe_2O_4/H_2O$.

6 Conclusion

The present analysis focuses the hybrid nanofluid flow on an exponentially extending surface. The nanoparticles of $CoFe_2O_4$ and TiO_2 are mixed in water to hybridize the fluid. Thermal flow rat involves the utilization of the Cattaneo–Christov heat flux model. The famous Buongiorno model has also used in this study. The mathematical model is evaluated by HAM. The concluding remarks are presented at the end of this analysis.

1) It is found that upsurge in magnetic factor augments the skin friction coefficients along both directions. Furthermore, the effect of magnetic parameter (M = 1.5) is 52% greater for hybrid nanofluid flow than for the pure water. However, the increasing magnetic parameter reduces the heat transfer rates of water, TiO_2-H_2O, $CoFe_2O_4-H_2O$, and $TiO_2-CoFe_2O_4/H_2O$. Additionally, the greatest reducing behavior is found for $TiO_2-CoFe_2O_4/H_2O$.
2) The increasing thermophoresis parameter increases the heat transfer rates of water, TiO_2-H_2O, $CoFe_2O_4-H_2O$, and $TiO_2-CoFe_2O_4/H_2O$, while the increasing Brownian motion factor diminishes the heat transfer rates of pure water, TiO_2-H_2O, $CoFe_2O_4-H_2O$, and $TiO_2-CoFe_2O_4/H_2O$. The increasing effect of thermophoresis parameter (Nt = 0.4) is 39% higher for hybrid nanofluid than for the pure fluid. On the contrary, the declining impact of Brownian motion factor (Nb = 0.4) is 48% higher in case of hybrid nanofluid.
3) The increasing magnetic parameter diminishes the velocity panels along both directions. Also, due to the greater electrical conductivity of fluid, the highest impact of magnetic parameter is found for hybrid nanofluid flow.
4) The increasing ratio of rate factor reduces the velocity distribution of the nanofluid and hybrid nanofluid in the x-direction and augments along the y-direction.
5) Increasing the thermophoresis, thermal Biot number, and Brownian motion factors raises the thermal panels of fluids, while increasing the thermal relaxation time lowers them.
6) The concentration distributions of fluid are reduced when the Brownian motion factor and Schmidt number increase.

Funding information: This study was supported by Project No. 129257 implemented with the support provided from the National Research, Development and Innovation Fund of Hungary, financed under the K 18 funding scheme. The authors extends their appreciation to the Deanship of Scientific Research at King Khalid University, Abha, Saudi Arabia, for funding this work through the Research Group Project under Grant Number (RGP.2/505/44).

Author contributions: All authors have accepted responsibility for the entire content of this manuscript and approved its submission.

Conflict of interest: The authors state no conflict of interest.

Data availability statement: The data that support the findings of this study are available from the corresponding author upon a reasonable request.

References

[1] Maxwell JC. A treatise on electricity and magnetism. Oxford: Clarendon Press; 1873.
[2] Hamilton RL, Crosser OK. Thermal conductivity of heterogeneous two-component systems. Ind Eng Chem Fundam. 1962;1:187–91.
[3] Choi S, Eastman J. Enhancing thermal conductivity of fluids with nanoparticles; 1995 [cited 2021 Sep 10]. https://www.osti.gov/biblio/196525.
[4] Sarkar J, Ghosh P, Adil A. A review on hybrid nanofluids: Recent research, development and applications. Renew Sustain Energy Rev. 2015;43:164–77.
[5] Nabil MF, Azmi WH, Hamid KA, Zawawi NNM, Priyandoko G, Mamat R. Thermo-physical properties of hybrid nanofluids and hybrid nanolubricants: a comprehensive review on performance. Int Commun Heat Mass Transf. 2017;83:30–9.
[6] Sajid MU, Ali HM. Thermal conductivity of hybrid nanofluids: a critical review. Int J Heat Mass Transf. 2018;126:211–34.
[7] Devi SPA, Devi SSU. Numerical investigation of hydromagnetic hybrid Cu–Al2O3/water nanofluid flow over a permeable stretching sheet with suction. Int J Nonlinear Sci Numer Simul. 2016;17:249–57.
[8] Zainal NA, Nazar R, Naganthran K, Pop I. MHD flow and heat transfer of hybrid nanofluid over a permeable moving surface in the presence of thermal radiation. Int J Numer Methods Heat Fluid Flow. 2020.
[9] Roy NC, Pop I. Flow and heat transfer of a second-grade hybrid nanofluid over a permeable stretching/shrinking sheet. Eur Phys J Plus. 2020;135:768.

[10] Sreedevi P, Reddy PS. Williamson hybrid nanofluid flow over swirling cylinder with Cattaneo–Christov heat flux and gyrotactic microorganism. Waves Random Complex Media. 2021;1–28.
[11] Babu DH, Reddy SH, Naidu KK, Narayana PVS, Venkateswarlu B. Numerical investigation for entropy-based magneto nanofluid flow over non-linear stretching surface with slip and convective boundary conditions. ZAMM-J Appl Math Mech für Angew Math und Mech. 2023;103:e202300006.
[12] Reddy PS, Sreedevi P. Effect of Cattaneo–Christov heat flux on heat and mass transfer characteristics of Maxwell hybrid nanofluid flow over stretching/shrinking sheet. Phys Scr. 2021;96:125237.
[13] Reddy PS, Sreedevi P. Flow and heat transfer analysis of carbon nanotubes based nanofluid flow inside a cavity with modified Fourier heat flux. Phys Scr. 2021;96:55215.
[14] Harish Babu D, Naidu KK, Deo S, Satya Narayana PV. Impacts of inclined Lorentz forces on hybrid CNTs over an exponentially stretching sheet with slip flow. Int J Model Simul. 2023;43:310–24.
[15] Harish Babu D, Venkateswarlu B, Sarojamma G, Satya Narayana PV. Coupled impression of radiative thermal flux and Lorentz force on the water carrying composite nanoliquid streaming past an elastic sheet. J Therm Sci Eng Appl. 2022;14:91002.
[16] Acharya N, Maity S, Kundu PK. Influence of inclined magnetic field on the flow of condensed nanomaterial over a slippery surface: the hybrid visualization. Appl Nanosci. 2020 [cited 2021 Nov 18];10:633–47. doi: 10.1007/s13204-019-01123-0. https://link.springer.com/article/.
[17] Khan U, Waini I, Ishak A, Pop I. Unsteady hybrid nanofluid flow over a radially permeable shrinking/stretching surface. J Mol Liq. 2021;331:115752.
[18] Zhang X-H, A. Algehyne E, G. Alshehri M, Bilal M, Khan MA, Muhammad T. The parametric study of hybrid nanofluid flow with heat transition characteristics over a fluctuating spinning disk. PLoS One. 2021 [cited 2021 Oct 26];16:e0254457, https://journals.plos.org/plosone/article?id=10.1371/journal.pone.0254457.
[19] Tassaddiq A. Impact of Cattaneo-Christov heat flux model on MHD hybrid nano-micropolar fluid flow and heat transfer with viscous and joule dissipation effects. Sci Rep. 2021 [cited 2021 Oct 21];11:1–14, https://www.nature.com/articles/s41598-020-77419-x.
[20] Usman M, Hamid M, Zubair T, Ul Haq R, Wang W. Cu-Al2O3/Water hybrid nanofluid through a permeable surface in the presence of nonlinear radiation and variable thermal conductivity *via* LSM. Int J Heat Mass Transf. 2018;126:1347–56.
[21] Kaska SA, Khalefa RA, Hussein AM. Hybrid nanofluid to enhance heat transfer under turbulent flow in a flat tube. Case Stud Therm Eng. 2019;13:100398.
[22] Crane LJ. Flow past a stretching plate. Z für Angew Math und Phys ZAMP. 1970;21:645–7.
[23] Bhattacharyya K. Boundary layer flow and heat transfer over an exponentially shrinking sheet. Chin Phys Lett. 2011;28:74701.
[24] Mat Yuzut NH. MHD boundary layer flow due to an exponentially stretching sheet with radiation effect in porous medium. Universiti Teknologi MARA; 2017.
[25] Waini I, Ishak A, Pop I. Mixed convection flow over an exponentially stretching/shrinking vertical surface in a hybrid nanofluid. Alex Eng J. 2020;59:1881–91.
[26] Ishak A. MHD boundary layer flow due to an exponentially stretching sheet with radiation effect. Sains Malaysiana. 2011;40:391–5.
[27] Abbas N, Shatanawi W, Abodayeh K. Computational analysis of MHD nonlinear radiation Casson hybrid nanofluid flow at vertical stretching sheet. Symmetry (Basel). 2022;14:1494.
[28] Abbas MI, El-Khatib AM, Dib MF, Mustafa HE, Sayyed MI, Elsafi M. Theoretical study of non-Newtonian micropolar nanofluid flow over an exponentially stretching surface with free stream velocity. Adv Mech Eng. 2022;14:16878132221107790.
[29] Abbas N, Shatanawi W. Heat and mass transfer of micropolar-Casson nanofluid over vertical variable stretching riga sheet. Energies. 2022;15:4945.
[30] Akbar NS, Tripathi D, Khan ZH, Bég OA. A numerical study of magnetohydrodynamic transport of nanofluids over a vertical stretching sheet with exponential temperature-dependent viscosity and buoyancy effects. Chem Phys Lett. 2016;661:20–30.
[31] Khan Z, Shah RA, Islam S, Jan B, Imran M, Tahir F. Heat transfer squeezed flow of Carreau fluid over a sensor surface with variable thermal conductivity: a numerical study. Results Phys. 2016;6:940–5.
[32] Sandeep N, Sulochana C, Kumar BR. Unsteady MHD radiative flow and heat transfer of a dusty nanofluid over an exponentially stretching surface. Eng Sci Technol Int J. 2016;19:227–40.
[33] Haq R, Nadeem S, Khan Z, Okedayo T. Convective heat transfer and MHD effects on Casson nanofluid flow over a shrinking sheet. Cent Eur J Phys. 2014;12:862–71.
[34] Ahmad S, Naveed Khan M, Rehman A, Felemban BF, Alqurashi MS, Alharbi FM, et al. Analysis of heat and mass transfer features of hybrid Casson nanofluid flow with the magnetic dipole past a stretched cylinder. Appl Sci. 2021;11:11203.
[35] Tassaddiq A, Khan S, Bilal M, Gul T, Mukhtar S, Shah Z, et al. Heat and mass transfer together with hybrid nanofluid flow over a rotating disk. AIP Adv. 2020;10:55317.
[36] Shanmugapriya M, Sundareswaran R, Senthil Kumar P. Heat and mass transfer enhancement of MHD hybrid nanofluid flow in the presence of activation energy. Int J Chem Eng. 2021;2021:1–12.
[37] Roy NC, Pop I. Heat and mass transfer of a hybrid nanofluid flow with binary chemical reaction over a permeable shrinking surface. Chin J Phys. 2022;76:283–98.
[38] Takabi B, Shokouhmand H. Effects of Al_2O_3–Cu/water hybrid nanofluid on heat transfer and flow characteristics in turbulent regime. Int J Mod Phys C. 2015;26:1550047.
[39] Santhi M, Suryanarayana Rao KV, Sudarsana Reddy P, Sreedevi P. Heat and mass transfer characteristics of radiative hybrid nanofluid flow over a stretching sheet with chemical reaction. Heat Transf. 50, 2021 [cited 2023 Sep 30]. p. 2929–49. https://onlinelibrary.wiley.com/doi/full/doi: 10.1002/htj.22012.
[40] Acharya N. On the flow patterns and thermal behaviour of hybrid nanofluid flow inside a microchannel in presence of radiative solar energy. J Therm Anal Calorim. 2020 [cited 2021 Nov 18];141:1425–42. doi: 10.1007/s10973-019-09111-w. https://link.springer.com/article/.
[41] Acharya N, Bag R, Kundu PK. On the impact of nonlinear thermal radiation on magnetized hybrid condensed nanofluid flow over a permeable texture. Appl Nanosci. 2020 [cited 2021 Nov 18];10:1679–91. doi: 10.1007/s13204-019-01224-w. https://link.springer.com/article/.
[42] Gupta S, Kumar D, Singh J. Magnetohydrodynamic three-dimensional boundary layer flow and heat transfer of water-driven copper and alumina nanoparticles induced by convective conditions. Int J Mod Phys B. 2019;33:1950307.

[43] Khan JA, Mustafa M, Hayat T, Sheikholeslami M, Alsaedi A. Three-dimensional flow of nanofluid induced by an exponentially stretching sheet: An application to solar energy. PLoS One. 2015;10:e0116603.
[44] Hayat T, Aziz A, Muhammad T, Alsaedi A. Three-dimensional flow of nanofluid with heat and mass flux boundary conditions. Chin J Phys. 2017;55:1495–510.
[45] Acharya N, Maity S, Kundu PK. Framing the hydrothermal features of magnetized TiO2–CoFe2O4 water-based steady hybrid nanofluid flow over a radiative revolving disk. Multidiscip Model Mater Struct. 2020;16:765–90.
[46] Ahmed J, Khan M, Ahmad L. Stagnation point flow of Maxwell nanofluid over a permeable rotating disk with heat source/sink. J Mol Liq. 2019;287:110853.
[47] Raju CSK, Sandeep N. Unsteady Casson nanofluid flow over a rotating cone in a rotating frame filled with ferrous nanoparticles: a numerical study. J Magn Magn Mater. 2017;421:216–24.
[48] Dawar A, Thumma T, Islam S, Shah Z. Optimization of response function on hydromagnetic buoyancy-driven rotating flow considering particle diameter and interfacial layer effects: Homotopy and sensitivity analysis. Int Commun Heat Mass Transf. 2023 [cited 2023 Apr 9];144:106770, https://linkinghub.elsevier.com/retrieve/pii/S0735193323001598.
[49] Liu I-C, Wang H-H, Peng Y-F. Flow and heat transfer for three-dimensional flow over an exponentially stretching surface. Chem Eng Commun. 2013;200:253–68.
[50] Magyari E, Keller B. Heat and mass transfer in the boundary layers on an exponentially stretching continuous surface. J Phys D Appl Phys. 1999;32:577–85.
[51] Ramzan M, Sheikholeslami M, Saeed M, Chung JD. On the convective heat and zero nanoparticle mass flux conditions in the flow of 3D MHD Couple Stress nanofluid over an exponentially stretched surface. Sci Rep. 2019;9:1–13.